Geophysical Research Letters

RESEARCH LETTER
10.1029/2019GL086627

Laboratory Study on Fluid-Induced Fault Slip Behavior: The Role of Fluid Pressurization Rate

Lei Wang[1,2], Grzegorz Kwiatek[1,2], Erik Rybacki[1], Audrey Bonnelye[1], Marco Bohnhoff[1,2], and Georg Dresen[1,3]

[1]Helmholtz Centre Potsdam, GFZ German Research Centre for Geosciences, Potsdam, Germany, [2]Department of Earth Sciences, Free University Berlin, Berlin, Germany, [3]Institute of Earth and Environmental Science, University of Potsdam, Potsdam, Germany

Key Points:
- Fluid-induced fault slip experiments have been conducted on critically stressed sandstone samples with saw-cut fractures
- Fluid-induced fault slip mode is controlled by fluid pressurization rate rather than by the magnitude of fluid pressure
- Independent of fault slip mode, we observed dynamic frictional weakening of the artificial fault at elevated pore pressure

Supporting Information:
- Supporting Information S1
- Movie S1
- Movie S2

Correspondence to:
L. Wang,
wanglei@gfz-potsdam.de

Citation:
Wang, L., Kwiatek, G., Rybacki, E., Bonnelye, A., Bohnhoff, M., & Dresen, G. (2020). Laboratory study on fluid-induced fault slip behavior: The role of fluid pressurization rate. *Geophysical Research Letters*, *47*, e2019GL086627. https://doi.org/10.1029/2019GL086627

Received 11 DEC 2019
Accepted 3 MAR 2020
Accepted article online 9 MAR 2020

Abstract Understanding the physical mechanisms governing fluid-induced fault slip is important for improved mitigation of seismic risks associated with large-scale fluid injection. We conducted fluid-induced fault slip experiments in the laboratory on critically stressed saw-cut sandstone samples with high permeability using different fluid pressurization rates. Our experimental results demonstrate that fault slip behavior is governed by fluid pressurization rate rather than injection pressure. Slow stick-slip episodes (peak slip velocity < 4 μm/s) are induced by fast fluid injection rate, whereas fault creep with slip velocity < 0.4 μm/s mainly occurs in response to slow fluid injection rate. Fluid-induced fault slip may remain mechanically stable for loading stiffness larger than fault stiffness. Independent of fault slip mode, we observed dynamic frictional weakening of the artificial fault at elevated pore pressure. Our observations highlight that varying fluid injection rates may assist in reducing potential seismic hazards of field-scale fluid injection projects.

Plain Language Summary Human-induced earthquakes from field-scale fluid injection projects including enhanced geothermal system and deep wastewater injection have been documented worldwide. Although it is clear that fluid pressure plays a crucial role in triggering fault slip, the physical mechanism behind induced seismicity still remains poorly understood. We performed laboratory tests, and here we present two fluid-induced slip experiments conducted on permeable Bentheim sandstone samples crosscut by a fault that is critically stressed. Fault slip is then triggered by pumping the water from the bottom end of the sample at different fluid injection rates. Our results show that fault slip is controlled by fluid pressure increase rate rather than by the absolute magnitude of fluid pressure. In contrast to episodes of relatively rapid but stable sliding events caused by a fast fluid injection rate, fault creep is observed during slow fluid injection. Strong weakening of the dynamic friction coefficient of the experimental fault is observed at elevated pore pressure, independent of fault slip mode. These results may provide a better understanding of the complex behavior of fluid-induced fault slip on the field scale.

1. Introduction

Induced seismicity associated with fluid injection has been reported worldwide. For example, waste-water injection in Oklahoma resulted in induced seismicity with event magnitudes as large as M5 (Keranen et al., 2014). Also, stimulation of enhanced geothermal systems (Deichmann & Giardini, 2009; Olasolo et al., 2016) produced damaging earthquakes, and unconventional hydrocarbon reservoir (Ellsworth, 2013) generated earthquakes large enough to be felt. Pore fluid pressure plays an important role in triggering fault reactivation. Induced seismicity is understood as a manifestation of the effective stress principle in Coulomb failure. At increasing pore pressure, onset of fault instability may occur once the shear stress τ resolved along a fault plane exceeds the shear strength τ_p. This is commonly expressed by

$$\tau \geq \tau_p = C + \mu(\sigma_n - P_p), \quad (1)$$

where C is cohesion ($C \approx 0$ is often assumed for fault planes), μ is a friction coefficient ($0.6 \leq \mu \leq 0.85$ for most crustal rocks), σ_n is the normal stress acting on fault planes, and P_p is the pore pressure. In this context, the pore pressure build-up results in a corresponding reduction of effective normal stress σ_n' ($\sigma_n' = \sigma_n - P_p$)

that clamps the fault planes and thus promotes fault slip. Equation 1 above, however, is restricted to fault slip initiation caused by fluid overpressure, and the subsequent stability issue of frictional sliding (unstable or stable slip) still remains unknown.

To mitigate seismic hazard and risk associated with fluid injection, reduction of fluid injection rates or limiting injected volume has been widely adopted. The successful control of seismic activity during fluid injection in waste-water disposal (Langenbruch & Zoback, 2016) and enhanced geothermal projects (Kwiatek et al., 2019) by adjusting the injection parameters indicates that fault slip mode may be sensitive to volume, rate, and pressure of fluid injections. However, many geophysical and geodetic observations have shown that aseismic slip may contribute significantly to deformation during fluid injection, suggesting that faults may slide slowly and stably with no seismicity detected (Cappa et al., 2018, 2019; Guglielmi et al., 2015; McGarr & Barbour, 2018; Wei et al., 2015). The nucleation and evolution of induced fault rupture caused by pore pressure perturbations have been studied using fracture mechanics (Galis et al., 2017; Garagash & Germanovich, 2012; Viesca & Rice, 2012; Wang et al., 2016), rate and state friction (RSF)-based models (Heimisson et al., 2019), poroelastic coupling (Goebel et al., 2016, 2017; Segall & Lu, 2015), and earthquake interactions (Catalli et al., 2016). However, the physical mechanisms governing fault sliding modes in response to fluid pressurization are still a matter of debate.

A limited number of experimental studies were conducted to investigate fault sliding behavior induced by controlled fluid overpressure. Injection-induced slip experiments on granite with rough saw-cut fractures show that the occurrence of stepwise slip and temporal drops in pore pressure is associated with shear dilation (Nemoto et al., 2008). From triaxial shear experiments on permeable and impermeable sandstones with saw-cut fractures, Rutter and Hackston (2017) demonstrated that dynamic slip may be easily generated by fluid pressurization in the case of a less permeable rock matrix. Creep experiments conducted on carbonate-bearing and shale-bearing fault gouges by increasing pore pressure under conditions of constant shear stress indicate that dynamic slip instability may be triggered, even if fault friction is characterized by rate-strengthening behavior (Scuderi et al., 2017; Scuderi & Collettini, 2018). French Melodie et al. (2016) performed axial compression and lateral relaxation tests on permeable sandstones with saw-cut surfaces. Their results illustrate that fluid pressurization is less effective than a reduction of confining pressure in initiating accelerated fault sliding. By stepwise increasing fluid pressure into faulted granite samples with different roughness at constant piston position (i.e., stress relaxation test), rapid slip is induced on rough fractures (Ye & Ghassemi, 2018). Moreover, fluid injection into a saw-cut granite sample in stress relaxation test shows that the onset of fault activation may not be predicted by equation 1 at high injection rates. This is presumably caused by a significantly heterogeneous distribution of fluid pressure on the fault plane (Noël et al., 2019; Passelègue et al., 2018).

The objective of this study is to unravel the slip characteristics of a critically stressed fault associated with fluid pressurization. We conducted injection-induced fault slip experiments on saw-cut permeable Bentheim sandstones using different fluid injection schemes. We highlight that fluid pressurization rate controls fault slip mode in addition to the magnitude of fluid pressure pulses.

2. Materials and Methods

To eliminate the potential influence of heterogeneous pore pressure distribution due to a local gradient in fluid pressure on induced fault slip, two isotropic and homogeneous Bentheim sandstone samples with initial porosity of ~23% and high permeability of ~1 Darcy were used (Wang et al., 2020). The estimated diffusion time $t_c < 5 \times 10^{-3}$ s (see Text S1 of the supporting information) suggests that fluid pressure within the sample equilibrates rapidly compared to the duration of the tests. Bentheim sandstone is mainly composed of quartz minerals (96.5%) with an average grain size of ~200 μm. Cylindrical samples with dimensions of 50-mm diameter × 100-mm length were prepared with a saw-cut fracture oriented at $\theta = 30°$ to the cylinder axis, displaying an elliptical fault interface of 50 mm in width and 100 mm in length along strike. Fault surfaces of two samples were then polished with the same surface grinder, ensuring that they have the similar surface roughness (see Figures S1 and S2 and Table S1).

Two pairs of orthogonal strain gages were attached at the center of upper and lower sample blocks for measurement of vertical and horizontal strain of the rock matrix. We also glued four strain gages (SGF1-SGF4) at ~3 mm distance to the saw-cut fault to monitor the deformation during sliding

(Figure S3). Subsequently, the saw-cut sample was encapsulated by a rubber jacket to avoid the intrusion of confining oil. To simultaneously record acoustic emission (AE) events, 16 piezoelectric transducers (PZTs, resonance frequency ~1 MHz) contained in brass cases were directly mounted to the surface of samples, ensuring full azimuthal coverage for AE events (Figure S3). AE waveforms were amplified first by 40 dB using preamplifiers equipped with 100-kHz high-pass filters and then recorded at a sampling rate of 10 MHz with 16-bit amplitude resolution. Ultrasonic P-wave velocities along different traveling paths were also measured repeatedly throughout the experiment using a periodic ultrasonic transmission technique in which a rectangular electrical pulse with 100-V amplitude and 3 μs duration was emitted by PZTs at 10 s time interval and the remaining sensors served as receivers. P-wave arrival time is automatically picked using a series of picking algorithms including the Akaike information criterion (Stanchits et al., 2011). Considering the potential stress-induced anisotropy, an updated anisotropic velocity model consisting of five horizontal layers and one vertical layer was used to locate AE activity by minimizing travel-time residuals using a downhill simplex algorithm, resulting in a hypocenter location accuracy of ±2 mm.

Experiments were conducted at room temperature using a servo-hydraulic triaxial deformation apparatus (MTS, stiffness of machine plus assembly $\approx 0.65 \times 10^9$ N/m or ~330 MPa/mm) equipped with a pore pressure system (Quizix 6000) (see Figure S4). Tests were performed in consecutive steps as follows. First, samples were loaded hydrostatically up to the desired confining pressure (σ_3) of 35 MPa while pore pressure (P_p) was maintained constant at 5 MPa, allowing for sample compaction. Subsequently, axial load was applied at a displacement rate of 1 μm/s to obtain the shear strength (τ_{ss}) along the fault plane. Next, axial load was reduced slowly with a displacement rate of 0.05 μm/s, so that the calculated shear stress (τ) equals $0.92 \times \tau_{ss}$. From this point on, we kept the position of the axial hydraulic cylinder constant, and finally pumped distilled water into the samples to induce fault slip. Note that confining pressure σ_3 remained constant at 35 MPa throughout fluid injection.

P_p was applied from the bottom end of the sample by advancing the down-stream syringe pump while the top end of the sample was connected to a closed reservoir, resulting in undrained boundary condition (Figure S5). To investigate the correlation between fault slip and fluid pressure, we applied two different fluid injection schemes (hereafter tests "SC1" and "SC2", respectively). P_p was increased stepwise from 5 to 29 MPa with a rate of 2 MPa/min in test SC1 and 0.5 MPa/min in test SC2 (Figure S6). Each fluid injection phase lasted for 10 min. For tests SC1 and SC2, fluid pressure was increased stepwise by 4 MPa, with each step lasting 2 and 8 min, respectively. Subsequently, P_p was held constant for 8 and 2 min for tests SC1 and SC2, respectively.

We measured axial stress (σ_1) using an internal load cell with an accuracy of ±0.05 MPa. In addition, total axial displacement was determined using an external linear-variable displacement transducer (LVDT) located outside of the pressure vessel. Throughout the experiment, mechanical and hydraulic data were all synchronously monitored with a sampling rate of 10 Hz.

Shear stress (τ) and effective normal stress (σ_n') resolved on the saw-cut fault plane are estimated by

$$\tau = (\sigma_1 - \sigma_3)\sin\theta\cos\theta, \tag{2}$$

$$\sigma_n' = (\sigma_3 - P_p) + (\sigma_1 - \sigma_3)\sin^2\theta. \tag{3}$$

Note that τ and σ_n' were corrected for the reduction of elliptical contact area between the two saw-cut blocks during axial deformation (see Text S2). In addition, fault slip (s) was determined from total axial displacement measured by the LVDT (Δl_{LVDT}) minus deformation of the loading frame (Δl_{MTS}) and rock matrix (Δl_{RM}), as given by

$$s = \frac{\Delta l_{LVDT} - \Delta l_{MTS} - \Delta l_{RM}}{\cos\theta}. \tag{4}$$

Δl_{RM} was estimated using $\Delta l_{RM} = \varepsilon_1 L$ in which ε_1 is the mean axial strain of two vertical strain gages glued to the rock specimen surfaces and L is sample length.

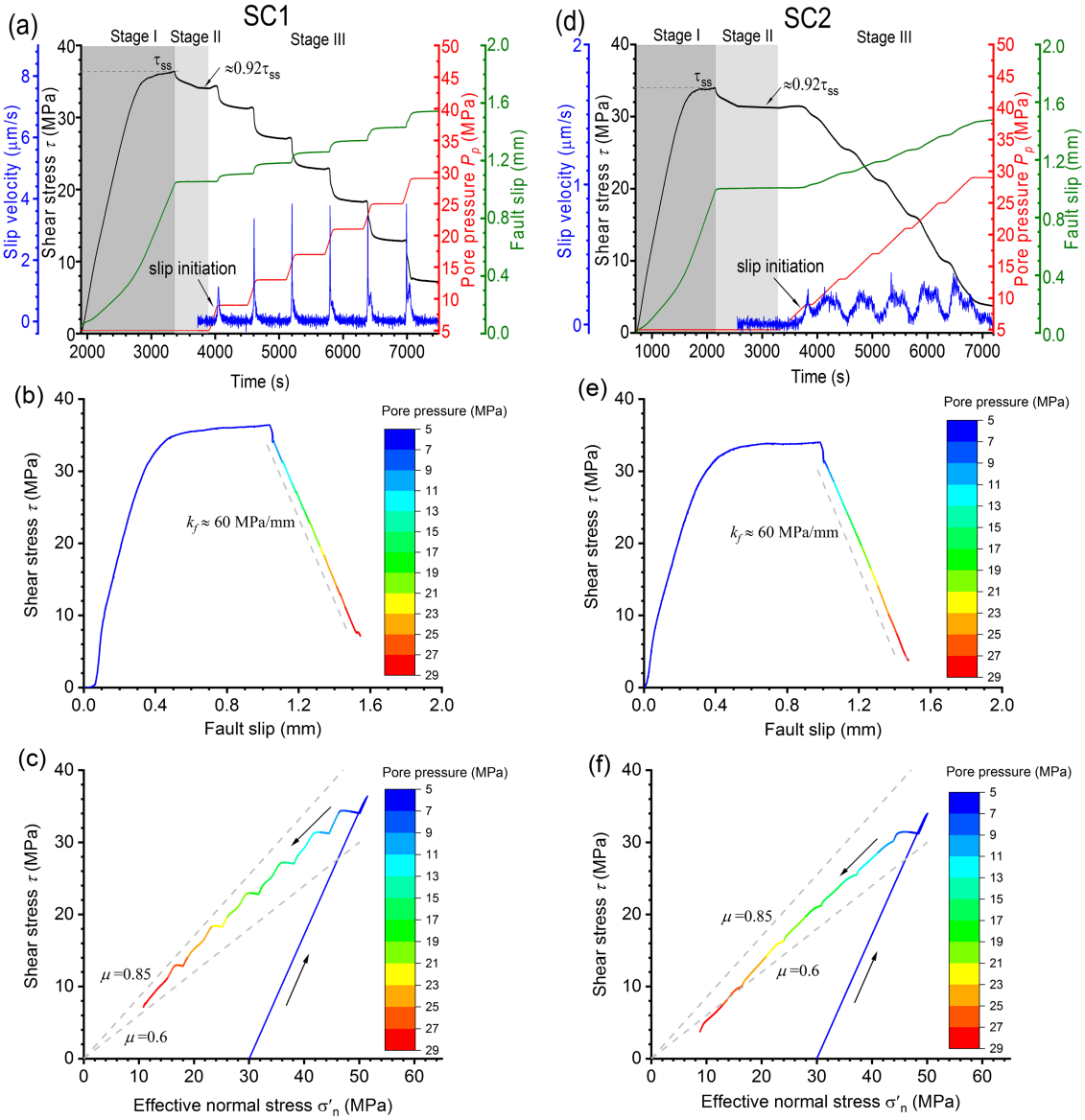

Figure 1. Time history of fluid pressure, shear stress, fault slip, and slip velocity measured in test SC1 (a) and test SC2 (d) at a constant confining pressure of 35 MPa. After the shear strength (τ_{ss}) at steady state was achieved (Stage I), shear stress was then reduced to about 0.92 × τ_{ss} (Stage II). Finally, fluid pressure was applied to saw-cut samples at a fluid pressurization rate of 2 MPa/min in test SC1 and of 0.5 MPa/min in test SC2, respectively (Stage III). Note that the scale bars for slip velocity in (a) and (d) are different. Measured shear stress vs. fault slip from Stage I to Stage III in test SC1 (b) and SC2 (e). Using the linear-regression technique (broken lines), the estimated values of fault stiffness (k_f) during fluid injection for both saw-cut samples are equal to about 60 MPa/mm. Relation between shear stress and effective normal stress from Stage I to Stage III in test SC1 (c) and SC2 (f). Note that the curves are color coded by the applied pore pressure (Figures 1b, 1c, 1e, and 1f).

3. Results

3.1. Mechanical Stability of Fault Slip

During the initial loading stage, shear stress τ resolved on the fault plane first shows an almost linear increase with progressively faster fault slip (Figures 1a and 1d). Between a clearly visible yield point and peak shear stress (shear strength τ_{ss}), slip increased linearly. For a confining pressure of σ_3 = 35 MPa and pore pressure of P_p = 5 MPa, the values of τ_{ss} are very similar for both tests (i.e., $\tau_{ss} \approx 36$ MPa and $\tau_{ss} \approx 34$ MPa in tests SC1 and SC2, respectively). τ was then reduced to about 0.92×τ_{ss} prior to injection. We observed an initial linear increase in τ preceding injection-induced slip initiation (Figures 1a, 1d, 2a, and 2e), likely indicating expansion of the sample due to injection at undrained conditions. Interestingly,

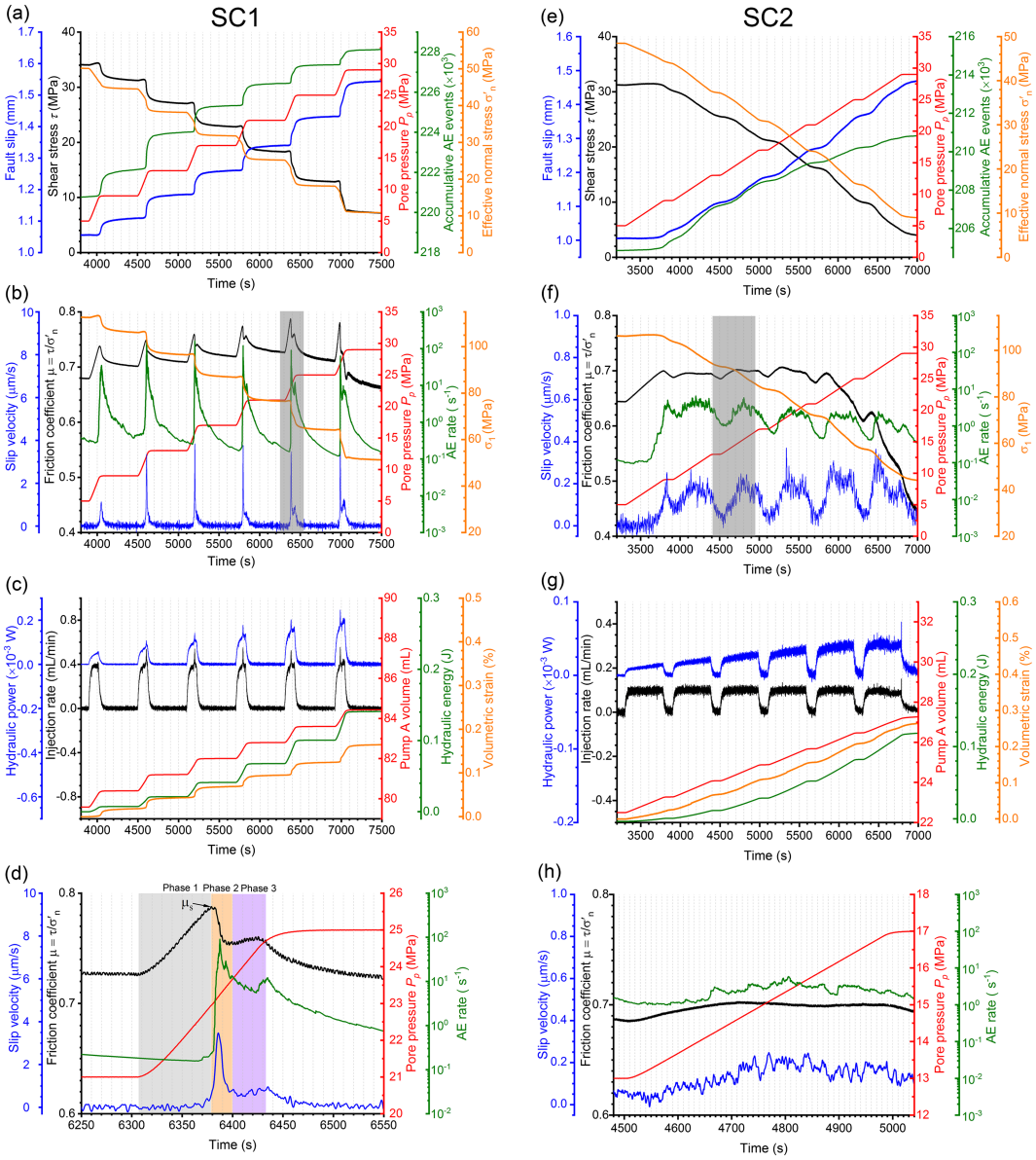

Figure 2. Time history of fault slip, shear stress, pore pressure, accumulative AE events, and effective normal stress since fluid injection in test SC1 (a) and SC2 (e). Time history of slip velocity, frictional coefficient, AE rate, and axial stress in test SC1 (b) and SC2 (f). Time history of injection rate, injection fluid volume, hydraulic power, hydraulic energy, and volumetric strain (compaction is negative) of rock matrix in test SC1 (c) and SC2 (g). Enlarged view of shaded area in Figure 2b shows that one slow stick-slip event during fast fluid pressurization may be divided into three phases (d). Enlarged view of shaded area in Figure 2f shows fault creep behavior during slow fluid pressurization in detail (h).

both critically stressed saw-cut samples started to slide towards the end of the first fluid injection stage (at $P_p \approx 8.5$ MPa), suggesting that the magnitude of fluid pressure controls fault slip initiation, as predicted by equation 1. Slow stick-slip episodes (slow stick-slip events are defined as having peak slip velocities <1 mm/s) occur at the fast fluid pressurization rate applied in test SC1. Slip abruptly accelerated to peak velocity and then decelerated slowly. In contrast, almost continuous fault creep was observed at fluid injection rates that were four times slower in test SC2. This suggests that fluid pressurization rate controls fault slip mode.

Seismic (unstable) slip for natural faults generally shows high slip velocities (≥0.1 m/s) (Bürgmann, 2018). In test SC1, episodic slow stick-slip events were observed with slip velocities <4 μm/s over long slip durations >60 s (Figure S7). Slip remained episodic at low pressure rates in test SC2 with similar total fault

displacement (Figures 1a and 1d), but slip rates increased and decreased more slowly with maximum value <0.4 μm/s. After injection-induced slip initiates, τ progressively decreased with increasing fault slip s (Figures 1b and 1e). The estimated fault stiffness is $k_f \approx 60$ MPa/mm ($k_f = -\Delta\tau/\Delta s$) for both tests, irrespective of slip mode. For unstable fault slip to occur, the unloading stiffness of the loading system k_s needs to be smaller than the fault stiffness k_f (i.e., ratio $\kappa = k_s/k_f < 1$) (Rice & Rudnicki, 1979). Additionally, 2D analysis of the instability nucleation of a linear slip-weakening fault (Uenishi & Rice, 2003) suggests a critical nucleation length (L_c) of $L_c \approx 1.158G/k_f$, where G is the shear modulus of Bentheim sandstone (~11 GPa; see Text S3). The estimated L_c is about 220 mm, exceeding the sample size. Since k_s (≈330 MPa/mm) is larger than k_f, fault slip behavior for both tests is mechanically stable, in agreement with previous in situ and laboratory experiments in which fluid pressure may promote stable and slow slip (Cappa et al., 2019; French Melodie et al., 2016; French & Zhu, 2017; Guglielmi et al., 2015).

3.2. Frictional Behavior of Fault Slip

From the different progressive slip episodes at stepwise increased fluid pressure, we can estimate the evolution of friction coefficient $\mu = \tau/\sigma_n'$. Our results indicate that μ varies slightly between slip episodes and between tests SC1 and SC2 but is generally between 0.6 and 0.85 (Figures 1c, 1f, 2b, and 2f), in agreement with Byerlee's law (Byerlee, 1978). During fluid pressurization in test SC1, μ appears to slightly increase up to a static friction coefficient (μ_s) just before onset of sliding (Phase 1 in Figure 2d). μ then dropped rapidly as fault sliding accelerated to maximum sliding velocity (Phase 2 in Figure 2d). After sliding velocity decelerated to relatively steady value of about 0.6 μm/s followed by a slight growth with a duration of about 20 to 30 s, friction coefficient μ shows a slight rise (Phase 3 in Figure 2d). In test SC1, injection was stopped shortly after the onset of fault slip during the first and second fluid injection stages, and thus, there was no sufficient time to enter Phase 3, which was observed in the remaining four fluid injection stages (Figure 2b). Finally, after shut in, μ was reduced gradually, coinciding with a slower slip velocity (Figure 2b). From the relation between a relatively steady-state slip velocity and the corresponding dynamic friction coefficient in Phase 3 and the subsequent shut-in stage (Figure S8), we may infer that the samples initially exhibit rate-strengthening behavior. During the first four fluid injection stages, friction is not affected by slip (Figure S8). In contrast, friction shows a dramatic decrease with fault slip in the last fluid injection stage.

In contrast to test SC1, in SC2 initial friction coefficient of $\mu \approx 0.65$ increased to $\mu_s \approx 0.7$ towards the end of the first fluid injection stage when fault slip started. μ then remains almost constant during continuous fault creep (Figures 2f and 2h) at a slip velocity of <0.4 μm/s. Friction is only slightly modulated by increasing or decreasing slip velocity. Similar to test SC1, slip weakening was observed towards the end of test SC2.

3.3. Acoustic Emission Characteristics

The produced AE events are primarily distributed along the fault planes with a layer thickness of <5 mm (Figure S9), reflecting grain fracturing adjacent to the fault surfaces during ongoing sliding. Cumulative AE activity is clearly correlated with sliding, independent of slip mode (Figures 2a and 2e). The AE rate scales with slip velocity (Figures 2b and 2f). Slip requires breaking grain-scale asperities along the sliding surface, resulting in the generation of AE activity. We analyzed AE source types using average first motion polarities (pol) of P-wave first motion A_i recorded by a total of n sensors for one AE event (Zang et al., 1998), as given by $pol = \frac{1}{n}\sum_{i=1}^{n} \mathrm{sign}(A_i)$. AE event types are separated into tensile (T-type, $-1 \le pol < -0.25$), shear (S-type, $-0.25 \le pol \le 0.25$), and collapse (C-type, $0.25 < pol \le 1$) events, respectively. S-type events are dominant for the two faulted samples, accounting for about 70% of all events (Figures 3a and 3d).

To examine the effect of slip mode on the spatial distribution of generated AE hypocenters, we calculated the fractal dimension D for a set of N AE hypocenters using $r^D \propto C(r) = \frac{2}{N(N-1)} N_r(R < r)$, where $N_r(R < r)$ is the number of hypocenter pairs separated by a distance R lower than r (Hirata et al., 1987) (see Figure S10). A planar random point cloud has $D = 2$ while $D < 2$ indicates the localized damage patches (Hirata et al., 1987). Estimated D values for both tests are similar throughout fluid injection ($D < 2$), reflecting the spatial localization of AE event clouds (Figures 3b and 3e). This observation is supported by their accumulated AE hypocenter density distributions (Figures 3c and 3f), characterized by AE clusters concentrated at the upper right

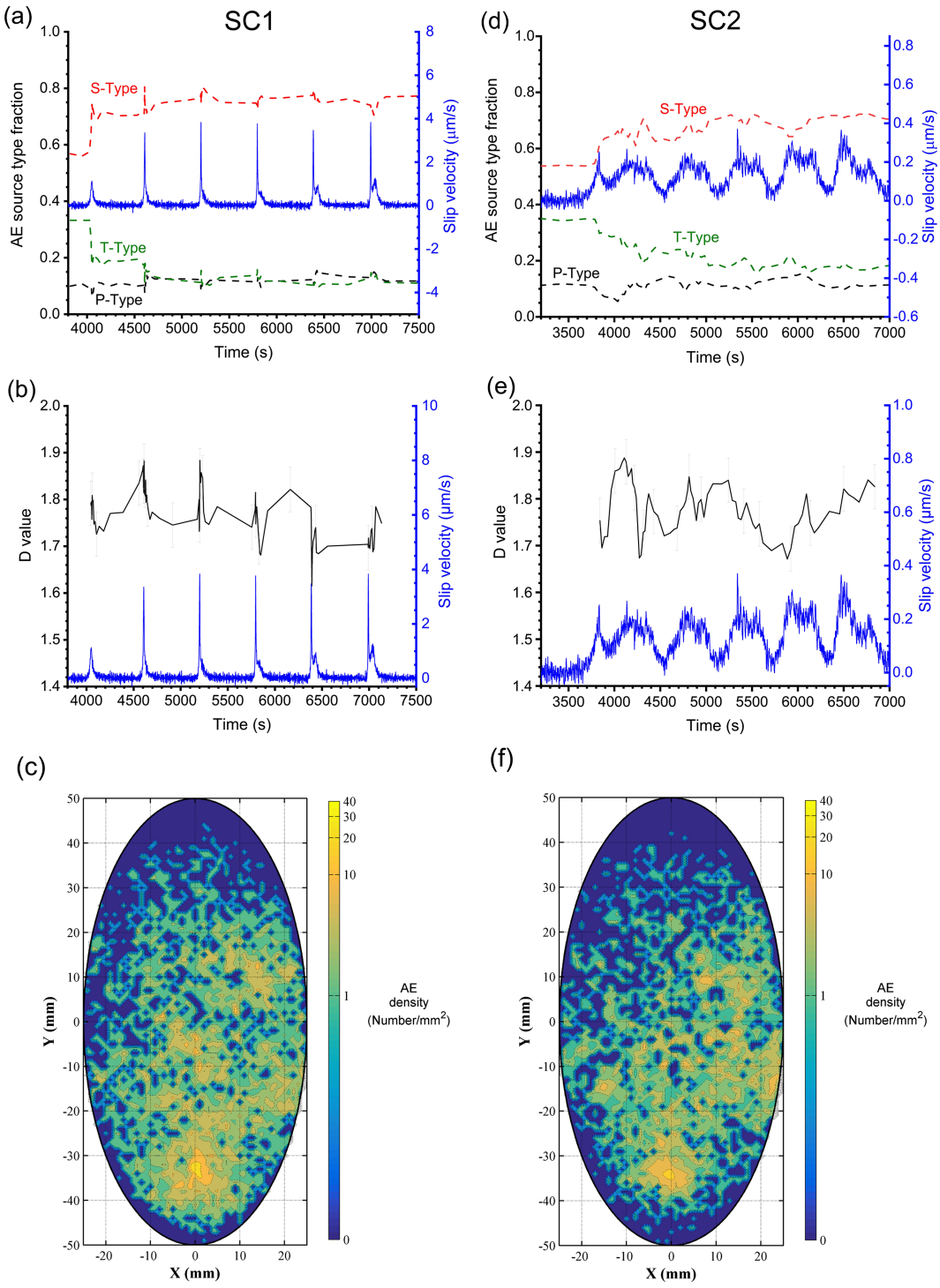

Figure 3. Time history of AE source type fraction (S-type, T-type, and P-type) evaluated using a moving window containing a constant number of 400 events with a running step of 80 events (80% overlap) in test SC1 (a) and SC2 (d). Time history of *D* value estimated by a moving window of 400 events with a running step of 80 events in test SC1 (b) and SC2 (e). The density distribution contour of accumulative AE hypocenters on the fault plane since fluid injection in test SC1 (c) and SC2 (f).

and lower parts of the fault plane. For both tests, the areas with highest AE density have similar locations, about 30 mm downward from the center. The AE hypocenters in test SC1 display a broader distribution than in test SC2, but this difference is not significant.

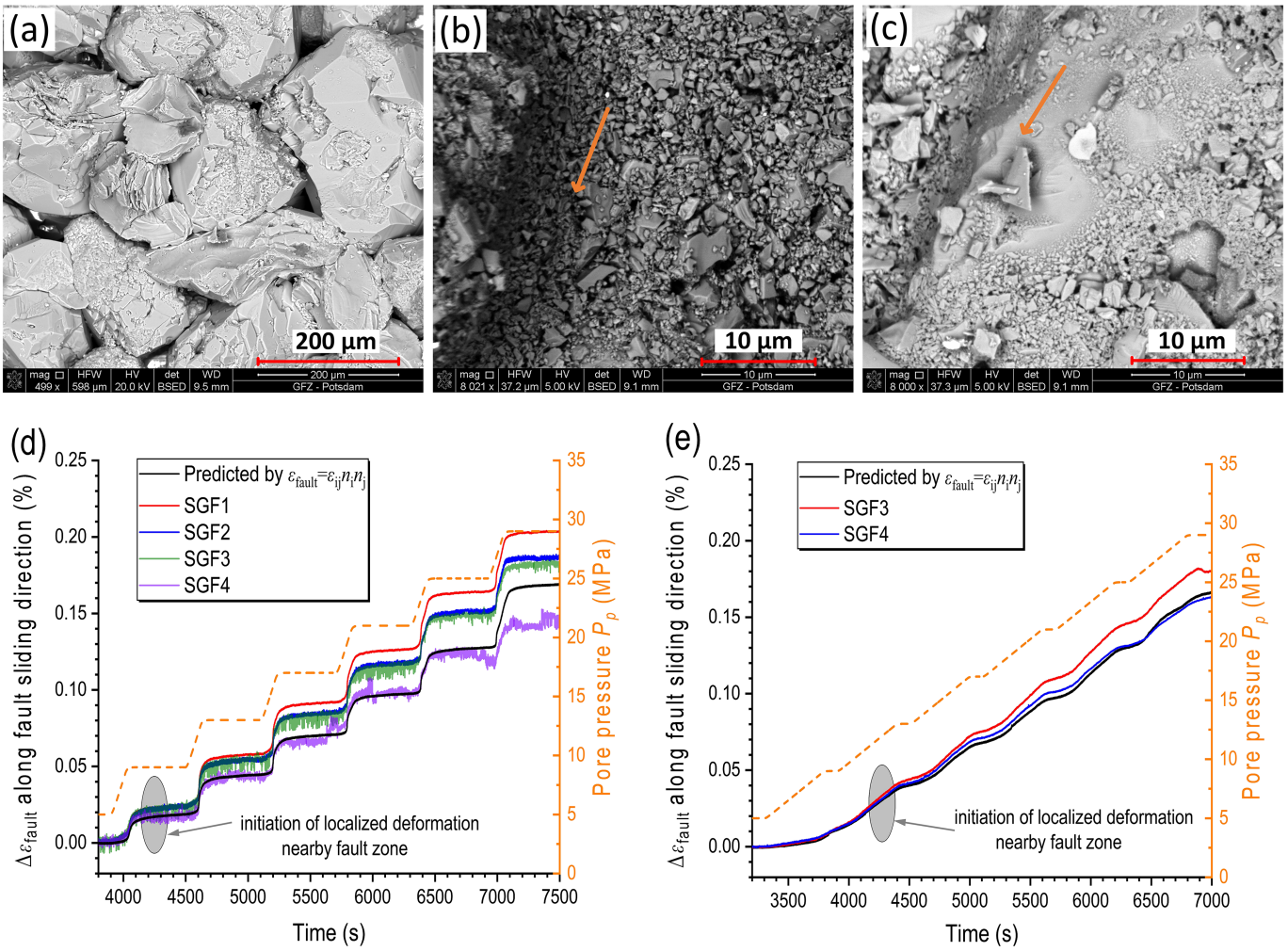

Figure 4. Microstructures of the fault surface before and after testing obtained by scanning electron microscopy (SEM). Initial bare fault surface characterized by distributed large quartz grains with an average diameter of about 200 µm and the abundant void space between grains (a). The formation of fault gouge featured by striking striation and dramatic reduction of grain size after test SC1 (b) and SC2 (c). The development of microscopic grooves indicate the sliding direction (orange arrows). Measured change of strain (compaction is negative) along fault sliding direction determined from the four local strain gages (SGF1 to SGF4) after start of fluid injection in test SC1 (d) and SC2 (e). Black solid lines show the strain change predicted from recordings from the two pairs of orthogonal strain gages glued on rock matrix and broken orange lines show pore pressure history. Shaded area shows the deviation of the signals from each other, indicating the onset of localized deformation nearby the fault. Note that for test SC2, the signals of SGF1 and SGF2 are not shown here because they failed at the onset of testing.

3.4. Microstructural Observations

The postmortem microstructures of fault zone damage show that shear slip is accommodated by significant grain size reduction due to comminution and cataclasis (Figures 4a, 4b, and 4c), resulting in the generation of fault gouge (Figure S11). The original quartz grains are about 200 µm in diameter and are crushed into a powder composed of microsized to nanosized grains. The fine powder observed in test SC2 suggests that the comminution process occurs also during fault creep, supported by the appearance of the postmortem fault gouges generated in test SC2. The gouge patches are elongated along the sliding direction with a maximum layer thickness of <0.2 mm (Figures S1, S2, and S11). The patches are heterogeneously distributed on the bare surfaces, suggesting heterogeneous frictional properties across the faults (Guglielmi et al., 2015). The formation of this very thin gouge layer is expected not to significantly affect the permeability of the entire sample. We observed no melting structures in both tests, likely due to the low slip velocity.

3.5. Localized Deformation

We used four local strain gages to monitor localized deformation close to the fault. The measured strain is heterogeneous with deviations up to 40% (Figures 4d and 4e). The bulk deformation measured by two pairs of orthogonal strain gages attached to the rock matrix at larger distance from the fault plane may be treated as a benchmark to examine localized deformation occurring close to the fault zone. Assuming that the rock matrix (host rock in the fault architecture) deforms homogeneously, the strain change along fault sliding direction ($\Delta\varepsilon_{\text{fault}}$) may be predicted by $\Delta\varepsilon_{\text{fault}} = \Delta\varepsilon_{\text{ij}} n_{\text{i}} n_{\text{j}} = \Delta\varepsilon_1 \cos^2\theta + \Delta\varepsilon_2 \sin^2\theta$ (Jaeger et al., 2009) where ε_{ij} and n_{i} are the strain tensor and unit direction vector, respectively, and $\Delta\varepsilon_1$ and $\Delta\varepsilon_2$ are the changes of vertical strain and horizontal strain of rock matrix, respectively. Comparing the strain gage measurements suggests that strain and likely stresses close to the fault zone are heterogeneous, resulting in different amounts of local slip (Figures 4d and 4e). Strain relaxation near the fault plane is more pronounced compared to the host rock, possibly associated with accumulated damage in the vicinity of the fault zone. This is consistent with the field-scale observation for natural faults (Brenguier et al., 2008; Gao & Crampin, 2004).

4. Discussion

The spectrum of faulting behavior may be separated into stable creep, slow slip, and dynamic seismic slip (Ide et al., 2007; Ikari et al., 2013). Slow slip and fault creep are commonly thought to be aseismic. The slow stick-slip and fault creep due to fluid pressurization reproduced in our experiments may provide a better understanding of the main aseismic slip induced in the large-scale field hydraulic stimulation (De Barros et al., 2016; Guglielmi et al., 2015) and of slow slip events occurring in the regions of elevated fluid pressure at the plate boundary (Kodaira et al., 2004; Perfettini & Ampuero, 2008).

4.1. Effect of Fluid Injection on Frictional Behavior

Although we did not perform velocity-stepping experiments, the rate strengthening for Bentheim sandstone at initial conditions is inferred (see section 3.2), as widely observed on quartz-rich fault gouges (Tembe et al., 2010). Recent velocity-stepping experiments reveal that frictional property parameters of gouge-bearing experimental faults may vary with increasing fluid pressure (Scuderi & Collettini, 2016; Xing et al., 2019). Initial rate-strengthening ($a - b > 0$) behavior of carbonate fault gouge was observed to evolve during slip to rate weakening ($a - b < 0$) accommodated by a gradual reduction of critical slip distance D_{c} (Scuderi & Collettini, 2016). Conversely, Xing et al. (2019) found that the stabilizing effect is enhanced by increasing fluid pressure, characterized by a gradual increase in value of $a - b$ for four gouge materials. In our experiments, however, a rate dependence of friction tends to decrease with increasing fluid pressure. Instead, the fault displays slip-weakening behavior after sliding for >1.3 mm at elevated fluid pressure ($P_{\text{p}} > 25$ MPa) (Figure S8). Slip weakening is believed to be one potential mechanism for slow slip (Ikari et al., 2013). Dynamic frictional weakening may be explained by localized flash heating (FH) of asperity contacts, thermal pressurization (TP) of pore fluid, and/or elastohydrodynamic lubrication (EHL). In contrast to EHL, the mechanisms of FH and TP often occur at high slip velocities (> 1 mm/s) and at high normal stress (Di Toro et al., 2004; Viesca & Garagash, 2015). This indicates that FH and TP may be not the reason for the dynamic weakening observed in our tests, as supported by the absence of melting structures in the fault gouge. Fault weakening at elevated fluid pressure may be related to the combined effects of evolving fault gouge structure with sliding distance and decreasing effective normal stress associated with fluid pressurization. With larger the sliding distance, more fine-grained gouge particles were generated. The generation of a thin layer fault gouge in the presence of water potentially forming a gel or suspension resembling a highly viscous fluid may partly support normal stress acting between fault walls (Brodsky & Kanamori, 2001). This lubrication process is expected to result in a drop of friction beyond the critical slip distance (Cornelio et al., 2019; Di Toro et al., 2011; Reches & Lockner, 2010), as observed in wet gouges (Orellana et al., 2019; Sammis et al., 2011). Additionally, the real contact area between fault planes is expected to be reduced due to the gradual decrease of effective normal stress during fluid pressurization (Rubinstein et al., 2004). This suggests that frictional sliding at grain contacts may be dominated by rolling friction, exacerbating the frictional weakening at elevated fluid pressure.

4.2. Strain Energy Release Due to Fluid Injection

Hydraulic power (Q_i) supplied by a pump is given by $Q_i = P_p(t)U(t)$ where P_p and U are measured injection fluid pressure and injection rate, respectively. In addition, hydraulic energy (E_i) is determined by integrating Q_i over injection time interval $[t_1, t_2]$, as written by $E_i = \int_{t_1}^{t_2} P_p U dt$. During tests SC1 and SC2, a total hydraulic energy $E_i \approx 0.14$ J was injected (Figures 2c and 2g). However, hydraulic power applied in test SC1 was about two to four times larger compared to the test SC2. The onset of accelerated slip is accompanied by a spike in Q_i because the associated stress relaxation results in an abrupt increase in pore volume for sample SC1. In contrast, the linear increase of Q_i in test SC2 is due to a gradual increase of pore volume associated with stable fault creep. For a faulted sample, the abrupt accumulation of energy characterized by Q_i due to fast pressurization is expected to be quickly released in the form of accelerated slip whereas slow energy release by fault creep occurs in the case of slow fluid pressurization.

4.3. Poroelastic Coupling of Stress and Pore Pressure

We noticed that at the beginning of fluid injection, axial stress σ_1 and shear stress τ continuously increased prior to slip initiation in test SC1 (Figures 2a and 2b). This may result from dilation of pore space associated with fluid pressurization under undrained conditions, leading to expansion of the sample. During all fluid injection stages, the ratio $\Delta\sigma_1/\Delta P_p$ was found to be in the range between 0.2 and 0.3 for sample SC1 (Figure S12). The observed increase of stress due to fluid injection may be quantified by "pore pressure/stress coupling" (PSC). For uniaxial compaction of a laterally infinite reservoir, the steady-state expression of PSC (Engelder & Fischer, 1994; Wang et al., 2016) is given by $\Delta\sigma_1/\Delta P_p = \alpha(1-2\nu)/(1-\nu)$ where α and ν are Biot coefficient and Poisson's ratio, respectively. Based on our measured $\nu \approx 0.17$ and $\alpha \approx 0.6$ for Bentheim sandstone (see Text S3), the predicted ratio $\Delta\sigma_1/\Delta P_p$ is about 0.47, slightly larger than our measured values. This is possibly because constant axial displacement (rigid constraint) is assumed in the equation above, which is not strictly valid in our tests, considering the finite stiffness of the loading frame. In contrast to test SC1, in sample SC2, we did not observe a striking increment of τ and σ_1 during the fluid overpressure stages, except for the occurrence of $\Delta\sigma_1/\Delta P_p \approx 0.28$ during the first fluid overpressure stage preceding fault slip initiation (Figure S13). This may be because stress relaxation associated with continuous fault creep compensates for stress amplification caused by fluid pressurization.

4.4. Fluid Pressurization Rate Versus Fluid Pressure Diffusion

The spatiotemporal variation in fluid pressure within the fault zone may result from heterogeneous hydraulic conductivity, causing fault slip behavior during fluid pressurization to vary in space and time (Bachmann et al., 2012; Brodsky & Lajoie, 2013; Martínez-Garzón et al., 2014). In situ observations of fault displacement during fluid injection indicate that the fault permeability is enhanced as a result of the opening and dilation of fractures (Guglielmi et al., 2015). The increase of hydraulic fault conductivity during fluid injection facilitates fast fluid pressure diffusion and leads to fast spatial dissipation of energy. Furthermore, hydromechanical modeling illustrates that the enhancement of fault permeability favors the growth of an aseismic slip zone (Cappa et al., 2018). For less permeable fault structures, fault slip zone may outpace the pore fluid migration (Bhattacharya & Viesca, 2019; Cappa et al., 2019; Guglielmi et al., 2015). However, the spatial fluid pressure distribution is seldom monitored accurately in the field, making it difficult to distinguish the influence of fluid pressurization rate on induced fault slip from effects related to the magnitude of fluid pressure and the fluid diffusion process. In our experiments, fluid cannot escape into the far field and fluid pressure is expected to diffuse rapidly. This suggests that the fluid pressure distribution within the entire faulted sample remains homogenous, as supported by the observed almost equal fluid pressures monitored at the two ends of samples (maximum differential pressure $< 2 \times 10^{-3}$ MPa; see Figure S5).

5. Conclusions

We examined fluid-induced slip behavior for permeable faulted samples under different fluid pressurization rates on a laboratory scale. Fault slip is initiated by increasing fluid pressure. We find that the mode of fault slip is primarily controlled by fluid pressurization rate, in particular for permeable fault structures. Repeating slow stick-slip events (peak slip velocity < 4 μm/s) are induced by fast fluid pressurization rates in contrast to fault creep with slip velocity < 0.4 μm/s induced by low fluid pressurization rates. Both slow stick-slip and fault creep are found to be mechanically stable in our experimental setup. Independent of fault

slip modes, we observed dynamic frictional weakening of the artificial fault at elevated pore pressure. Polarity analysis of acoustic emission events indicates that shear failure is dominant (about 70% of all events) for both fault slip modes. Strain relaxation in the vicinity of fault zone is observed during fluid-induced fault slip.

Acknowledgments
The authors thank Stefan Gehrmann for sample preparation and Michael Naumann for assistance with laboratory experiments in MTS apparatus. Valerian Schuster is also appreciated for obtaining SEM images. L. Wang acknowledges China Scholarship Council for providing funding to perform this study at GFZ. The authors thank Editor Gavin Hayes, Associated Editor Ake Fagereng, and two anonymous reviewers for their constructive and valuable comments. This manuscript is accompanied by Supporting Information. The experimental data presented in this study are available at data repository online (https://doi.org/10.6084/m9.figshare.11948739.v2) or at GFZ Data Services (https://doi.org/10.5880/GFZ.4.2.2020.002).

References

Bachmann, C. E., Wiemer, S., Goertz-Allmann, B. P., & Woessner, J. (2012). Influence of pore-pressure on the event-size distribution of induced earthquakes. *Geophysical Research Letters*, *39*(9). https://doi.org/10.1029/2012GL051480

Bhattacharya, P., & Viesca, R. C. (2019). Fluid-induced aseismic fault slip outpaces pore-fluid migration. *Science*, *364*(6439), 464 LP–468. https://doi.org/10.1126/science.aaw7354

Brenguier, F., Campillo, M., Hadziioannou, C., Shapiro, N. M., Nadeau, R. M., & Larose, E. (2008). Postseismic relaxation along the San Andreas Fault at Parkfield from continuous seismological observations. *Science*, *321*(5895), 1478 LP–1481. https://doi.org/10.1126/science.1160943

Brodsky, E. E., & Kanamori, H. (2001). Elastohydrodynamic lubrication of faults. *Journal of Geophysical Research*, *106*(B8), 16,357–16,374. https://doi.org/10.1029/2001JB000430

Brodsky, E. E., & Lajoie, L. J. (2013). Anthropogenic seismicity rates and operational parameters at the Salton Sea Geothermal Field. *Science*, *341*(6145), 543 LP–546. https://doi.org/10.1126/science.1239213

Bürgmann, R. (2018). The geophysics, geology and mechanics of slow fault slip. *Earth and Planetary Science Letters*, *495*, 112–134. https://doi.org/10.1016/j.epsl.2018.04.062

Byerlee, J. (1978). Friction of rocks. *Pure and Applied Geophysics*, *116*(4), 615–626. https://doi.org/10.1007/BF00876528

Cappa, F., Guglielmi, Y., Nussbaum, C., & Birkholzer, J. (2018). On the relationship between fault permeability increases, induced stress perturbation, and the growth of aseismic slip during fluid injection. *Geophysical Research Letters*, *45*(20), 11,11–12,20. https://doi.org/10.1029/2018GL080233

Cappa, F., Scuderi, M. M., Collettini, C., Guglielmi, Y., & Avouac, J.-P. (2019). Stabilization of fault slip by fluid injection in the laboratory and in situ. *Science Advances*, *5*(3), eaau4065. https://doi.org/10.1126/sciadv.aau4065

Catalli, F., Rinaldi, A. P., Gischig, V., Nespoli, M., & Wiemer, S. (2016). The importance of earthquake interactions for injection-induced seismicity: Retrospective modeling of the Basel Enhanced Geothermal System. *Geophysical Research Letters*, *43*(10), 4992–4999. https://doi.org/10.1002/2016GL068932

Cornelio, C., Spagnuolo, E., Di Toro, G., Nielsen, S., & Violay, M. (2019). Mechanical behaviour of fluid-lubricated faults. *Nature Communications*, *10*(1), 1274. https://doi.org/10.1038/s41467-019-09293-9

De Barros, L., Daniel, G., Guglielmi, Y., Rivet, D., Caron, H., Payre, X., et al. (2016). Fault structure, stress, or pressure control of the seismicity in shale? Insights from a controlled experiment of fluid-induced fault reactivation. *Journal of Geophysical Research: Solid Earth*, *121*(6), 4506–4522. https://doi.org/10.1002/2015JB012633

Deichmann, N., & Giardini, D. (2009). Earthquakes induced by the stimulation of an enhanced geothermal system below Basel (Switzerland). *Seismological Research Letters*, *80*(5), 784–798. https://doi.org/10.1785/gssrl.80.5.784

Di Toro, G., Goldsby, D. L., & Tullis, T. E. (2004). Friction falls towards zero in quartz rock as slip velocity approaches seismic rates. *Nature*, *427*(6973), 436–439. https://doi.org/10.1038/nature02249

Di Toro, G., Han, R., Hirose, T., De Paola, N., Nielsen, S., Mizoguchi, K., et al. (2011). Fault lubrication during earthquakes. *Nature*, *471*(7339), 494–498. https://doi.org/10.1038/nature09838

Ellsworth, W. L. (2013). *Injection-Induced Earthquakes. Science*, *341*(6142), 1225942. https://doi.org/10.1126/science.1225942

Engelder, T., & Fischer, M. P. (1994). Influence of poroelastic behavior on the magnitude of minimum horizontal stress, S_h in overpressured parts of sedimentary basins. *Geology*, *22*(10), 949–952. https://doi.org/10.1130/0091-7613(1994)022<0949:IOPBOT>2.3.CO;2

French, M. E., & Zhu, W. L. (2017). Slow fault propagation in serpentinite under conditions of high pore fluid pressure. *Earth and Planetary Science Letters*, *473*, 131–140. https://doi.org/10.1016/j.epsl.2017.06.009

French Melodie, E., Zhu, W., & Banker, J. (2016). Fault slip controlled by stress path and fluid pressurization rate. *Geophysical Research Letters*, *43*(9), 4330–4339. https://doi.org/10.1002/2016GL068893

Galis, M., Ampuero, J. P., Mai, P. M., & Cappa, F. (2017). Induced seismicity provides insight into why earthquake ruptures stop. *Science Advances*, *3*(12), eaap7528. https://doi.org/10.1126/sciadv.aap7528

Gao, Y., & Crampin, S. (2004). Observations of stress relaxation before earthquakes. *Geophysical Journal International*, *157*(2), 578–582. https://doi.org/10.1111/j.1365-246X.2004.02207.x

Garagash, D. I., & Germanovich, L. N. (2012). Nucleation and arrest of dynamic slip on a pressurized fault. *Journal of Geophysical Research*, *117*(B10). https://doi.org/10.1029/2012JB009209

Goebel, T. H. W., Hosseini, S. M., Cappa, F., Hauksson, E., Ampuero, J. P., Aminzadeh, F., & Saleeby, J. B. (2016). Wastewater disposal and earthquake swarm activity at the southern end of the Central Valley, California. *Geophysical Research Letters*, *43*(3), 1092–1099. https://doi.org/10.1002/2015GL066948

Goebel, T. H. W., Weingarten, M., Chen, X., Haffener, J., & Brodsky, E. E. (2017). The 2016 Mw5.1 Fairview, Oklahoma earthquakes: Evidence for long-range poroelastic triggering at >40 km from fluid disposal wells. *Earth and Planetary Science Letters*, *472*, 50–61. https://doi.org/10.1016/j.epsl.2017.05.011

Guglielmi, Y., Cappa, F., Avouac, J.-P., Henry, P., & Elsworth, D. (2015). Seismicity triggered by fluid injection–induced aseismic slip. *Science*, *348*(6240), 1224 LP–1226. https://doi.org/10.1126/science.aab0476

Heimisson, E. R., Dunham, E. M., & Almquist, M. (2019). Poroelastic effects destabilize mildly rate-strengthening friction to generate stable slow slip pulses. *Journal of the Mechanics and Physics of Solids*, *130*, 262–279. https://doi.org/10.1016/j.jmps.2019.06.007

Hirata, T., Satoh, T., & Ito, K. (1987). Fractal structure of spatial distribution of microfracturing in rock. *Geophysical Journal International*, *90*(2), 369–374. https://doi.org/10.1111/j.1365-246X.1987.tb00732.x

Ide, S., Beroza, G. C., Shelly, D. R., & Uchide, T. (2007). A scaling law for slow earthquakes. *Nature*, *447*(7140), 76. Retrieved from–79. https://doi.org/10.1038/nature05780

Ikari, M. J., Marone, C., Saffer, D. M., & Kopf, A. J. (2013). Slip weakening as a mechanism for slow earthquakes. *Nature Geoscience*, *6*(6), 468–472. https://doi.org/10.1038/ngeo1818

Jaeger, J. C., Cook, N. G. W., & Zimmerman, R. (2009). *Fundamentals of rock mechanics*. n/a: John Wiley & Sons.

Keranen, K. M., Weingarten, M., Abers, G. A., Bekins, B. A., & Ge, S. (2014). Sharp increase in central Oklahoma seismicity since 2008 induced by massive wastewater injection. *Science*, *345*(6195), 448 LP–451. https://doi.org/10.1126/science.1255802

Kodaira, S., Iidaka, T., Kato, A., Park, J.-O., Iwasaki, T., & Kaneda, Y. (2004). High pore fluid pressure may cause silent slip in the Nankai Trough. *Science*, *304*(5675), 1295–1298. https://doi.org/10.1126/science.1096535

Kwiatek, G., Saarno, T., Ader, T., Bluemle, F., Bohnhoff, M., Chendorain, M., et al. (2019). Controlling fluid-induced seismicity during a 6.1-km-deep geothermal stimulation in Finland. *Science Advances*, *5*(5), eaav7224. https://doi.org/10.1126/sciadv.aav7224

Langenbruch, C., & Zoback, M. D. (2016). How will induced seismicity in Oklahoma respond to decreased saltwater injection rates? *Science Advances*, *2*(11), e1601542. https://doi.org/10.1126/sciadv.1601542

Martínez-Garzón, P., Kwiatek, G., Sone, H., Bohnhoff, M., Dresen, G., & Hartline, C. (2014). Spatiotemporal changes, faulting regimes, and source parameters of induced seismicity: A case study from The Geysers geothermal field. *Journal of Geophysical Research: Solid Earth*, *119*(11), 8378–8396. https://doi.org/10.1002/2014JB011385

McGarr, A., & Barbour, A. J. (2018). Injection-induced moment release can also be aseismic. *Geophysical Research Letters*, *45*(11), 5344–5351. https://doi.org/10.1029/2018GL078422

Nemoto, K., Moriya, H., Niitsuma, H., & Tsuchiya, N. (2008). Mechanical and hydraulic coupling of injection-induced slip along pre-existing fractures. *Geothermics*, *37*(2), 157–172. https://doi.org/10.1016/j.geothermics.2007.11.001

Noël, C., Passelègue, F. X., Giorgetti, C., & Violay, M. (2019). Fault reactivation during fluid pressure oscillations: Transition from stable to unstable slip. *Journal of Geophysical Research: Solid Earth*, *124*(11), 10,940–10,953. https://doi.org/10.1029/2019JB018517

Olasolo, P., Juárez, M. C., Morales, M. P., D'Amico, S., & Liarte, I. A. (2016). Enhanced geothermal systems (EGS): A review. *Renewable and Sustainable Energy Reviews*, *56*, 133–144. https://doi.org/10.1016/j.rser.2015.11.031

Orellana, L. F., Giorgetti, C., & Violay, M. (2019). Contrasting mechanical and hydraulic properties of wet and dry fault zones in a proposed shale-hosted nuclear waste repository. *Geophysical Research Letters*, *46*(3), 1357–1366. https://doi.org/10.1029/2018GL080384

Passelègue, F. X., Brantut, N., & Mitchell, T. M. (2018). Fault reactivation by fluid injection: Controls from stress state and injection rate. *Geophysical Research Letters*, *45*(23), 12,812–837,846. https://doi.org/10.1029/2018GL080470

Perfettini, H., & Ampuero, J.-P. (2008). Dynamics of a velocity strengthening fault region: Implications for slow earthquakes and post-seismic slip. *Journal of Geophysical Research*, *113*(B9). https://doi.org/10.1029/2007JB005398

Reches, Z., & Lockner, D. A. (2010). Fault weakening and earthquake instability by powder lubrication. *Nature*, *467*(7314), 452–455. https://doi.org/10.1038/nature09348

Rice, J. R., & Rudnicki, J. W. (1979). Earthquake precursory effects due to pore fluid stabilization of a weakening fault zone. *Journal of Geophysical Research*, *84*(B5), 2177–2193. https://doi.org/10.1029/JB084iB05p02177

Rubinstein, S. M., Cohen, G., & Fineberg, J. (2004). Detachment fronts and the onset of dynamic friction. *Nature*, *430*(7003), 1005–1009. https://doi.org/10.1038/nature02830

Rutter, E., & Hackston, A. (2017). On the effective stress law for rock-on-rock frictional sliding, and fault slip triggered by means of fluid injection. *Philosophical Transactions of the Royal Society A: Mathematical, Physical and Engineering Sciences*, *375*(2103). https://doi.org/10.1098/rsta.2016.0001

Sammis, C. G., Lockner, D. A., & Reches, Z. (2011). The role of adsorbed water on the friction of a layer of submicron particles. *Pure and Applied Geophysics*, *168*(12), 2325–2334. https://doi.org/10.1007/s00024-011-0324-0

Scuderi, M. M., Collettini, C., & Marone, C. (2017). Frictional stability and earthquake triggering during fluid pressure stimulation of an experimental fault. *Earth and Planetary Science Letters*, *477*, 84–96. https://doi.org/10.1016/j.epsl.2017.08.009

Scuderi, M. M., & Collettini, C. (2016). The role of fluid pressure in induced vs. triggered seismicity: insights from rock deformation experiments on carbonates. *Scientific Reports*, *6*(1), 1. Retrieved from–9. https://doi.org/10.1038/srep24852

Scuderi, M. M., & Collettini, C. (2018). Fluid injection and the mechanics of frictional stability of shale-bearing faults. *Journal of Geophysical Research: Solid Earth*, *123*(10), 8364–8384. https://doi.org/10.1029/2018JB016084

Segall, P., & Lu, S. (2015). Injection-induced seismicity: Poroelastic and earthquake nucleation effects. *Journal of Geophysical Research: Solid Earth*, *120*(7), 5082–5103. https://doi.org/10.1002/2015JB012060

Stanchits, S., Mayr, S., Shapiro, S., & Dresen, G. (2011). Fracturing of porous rock induced by fluid injection. *Tectonophysics*, *503*(1–2), 129–145. https://doi.org/10.1016/j.tecto.2010.09.022

Tembe, S., Lockner, D. A., & Wong, T.-F. (2010). Effect of clay content and mineralogy on frictional sliding behavior of simulated gouges: Binary and ternary mixtures of quartz, illite, and montmorillonite. *Journal of Geophysical Research*, *115*(B3), B03416. https://doi.org/10.1029/2009JB006383

Uenishi, K., & Rice, J. R. (2003). Universal nucleation length for slip-weakening rupture instability under nonuniform fault loading. *Journal of Geophysical Research*, *108*(B1). https://doi.org/10.1029/2001JB001681

Viesca, R. C., & Garagash, D. I. (2015). Ubiquitous weakening of faults due to thermal pressurization. *Nature Geoscience*, *8*(11), 875–879. https://doi.org/10.1038/ngeo2554

Viesca, R. C., & Rice, J. R. (2012). Nucleation of slip-weakening rupture instability in landslides by localized increase of pore pressure. *Journal of Geophysical Research*, *117*(B3). https://doi.org/10.1029/2011JB008866

Wang, L., Bai, B., Li, X., Liu, M., Wu, H., & Hu, S. (2016). An analytical model for assessing stability of pre-existing faults in caprock caused by fluid injection and extraction in a reservoir. *Rock Mechanics and Rock Engineering*, *49*(7), 2845–2863. https://doi.org/10.1007/s00603-016-0933-0

Wang, L., Dresen, G., Rybacki, E., Bonnelye, A., & Bohnhoff, M. (2020). Pressure-dependent bulk compressibility of a porous granular material modelled by improved contact mechanics and micromechanical approaches: Effects of surface roughness of grains. *Acta Materialia*, *188*, 259–272. https://doi.org/10.1016/j.actamat.2020.01.063

Wei, S., Avouac, J.-P., Hudnut, K. W., Donnellan, A., Parker, J. W., Graves, R. W., et al. (2015). The 2012 Brawley swarm triggered by injection-induced aseismic slip. *Earth and Planetary Science Letters*, *422*, 115–125. https://doi.org/10.1016/j.epsl.2015.03.054

Xing, T., Zhu, W., French, M., & Belzer, B. (2019). Stabilizing effect of high pore fluid pressure on slip behaviors of gouge-bearing faults. *Journal of Geophysical Research: Solid Earth*, *124*(9), 9526–9545. https://doi.org/10.1029/2019JB018002

Ye, Z., & Ghassemi, A. (2018). Injection-induced shear slip and permeability enhancement in granite. *Journal of Geophysical Research: Solid Earth*, *123*(10), 9009–9032. https://doi.org/10.1029/2018JB016045

Zang, A., Christian Wagner, F., Stanchits, S., Dresen, G., Andresen, R., & Haidekker, M. A. (1998). Source analysis of acoustic emissions in Aue granite cores under symmetric and asymmetric compressive loads. *Geophysical Journal International*, *135*(3), 1113–1130. https://doi.org/10.1046/j.1365-246X.1998.00706.x